

REPORT DOCUMENTATION PAGE				Form Approved OMB No. 0704-0188	
<p>Public reporting burden for this collection of information is estimated to average 1 hour per response, including the time for reviewing instructions, searching existing data sources, gathering and maintaining the data needed, and completing and reviewing this collection of information. Send comments regarding this burden estimate or any other aspect of this collection of information, including suggestions for reducing this burden to Department of Defense, Washington Headquarters Services, Directorate for Information Operations and Reports (0704-0188), 1215 Jefferson Davis Highway, Suite 1204, Arlington, VA 22202-4302. Respondents should be aware that notwithstanding any other provision of law, no person shall be subject to any penalty for failing to comply with a collection of information if it does not display a currently valid OMB control number. PLEASE DO NOT RETURN YOUR FORM TO THE ABOVE ADDRESS.</p>					
1. REPORT DATE (DD-MM-YYYY) Apr 2014		2. REPORT TYPE Technical Paper		3. DATES COVERED (From - To) Apr 2014- June 2014	
4. TITLE AND SUBTITLE Exploration of POD-Galerkin Techniques for Developing Reduced Order Models of Reaction-Advection Equations				5a. CONTRACT NUMBER N/A	
				5b. GRANT NUMBER	
				5c. PROGRAM ELEMENT NUMBER	
6. AUTHOR(S) Huang, C., Anderson, W., Merkle, C. and Sankaran, V.				5d. PROJECT NUMBER	
				5e. TASK NUMBER	
				5f. WORK UNIT NUMBER Q12J	
7. PERFORMING ORGANIZATION NAME(S) AND ADDRESS(ES) Air Force Research Laboratory (AFMC) AFRL/RQR 5 Pollux Drive Edwards AFB CA 93524-7048				8. PERFORMING ORGANIZATION REPORT NO.	
9. SPONSORING / MONITORING AGENCY NAME(S) AND ADDRESS(ES) Air Force Research Laboratory (AFMC) AFRL/RQR 5 Pollux Drive Edwards AFB CA 93524-7048				10. SPONSOR/MONITOR'S ACRONYM(S)	
				11. SPONSOR/MONITOR'S REPORT NUMBER(S) AFRL-RQ-ED-TP-2014-146	
12. DISTRIBUTION / AVAILABILITY STATEMENT Distribution A: Approved for Public Release; Distribution Unlimited					
13. SUPPLEMENTARY NOTES Technical paper presented at 44th AIAA Fluid Dynamics Conference, Atlanta, GA, June 18, 2014. PA#14288					
14. ABSTRACT Galerkin's method is applied to reduce a high-order PDE system to a lower-order ODE system using POD eigen-basis to develop a reduced order model (ROM) describing the combustion response to acoustic excitations. A one-dimensional reaction-advection scalar equation is used as a representative equation to investigate the overall approach. Both linear and nonlinear model equations are employed to build the reduced order model. The influence of different discretization methods and time steps on the ROM are evaluated. Parametric explorations are performed to investigate the capabilities of the lower-order model for predicting combustion response.					
15. SUBJECT TERMS					
16. SECURITY CLASSIFICATION OF:			17. LIMITATION OF ABSTRACT SAR	18. NUMBER OF PAGES 26	19a. NAME OF RESPONSIBLE PERSON V. Sankaran
a. REPORT Unclassified	b. ABSTRACT Unclassified	c. THIS PAGE Unclassified			19b. TELEPHONE NO (include area code) 661-275-5534

Exploration of POD-Galerkin Techniques for Developing Reduced Order Models of Reaction-Advection Equations

Cheng Huang^{*}, William E. Anderson[†], Charles L. Merkle[‡]
Purdue University, West Lafayette, IN, 47907

and

Venkateswaran Sankaran[§]
Air Force Research Laboratory (AFRL), Edwards AFB, CA, 93524

Galerkin's method is applied to reduce a high-order PDE system to a lower-order ODE system using POD eigen-basis to develop a reduced order model (ROM) describing the combustion response to acoustic excitations. A one-dimensional reaction-advection scalar equation is used as a representative equation to investigate the overall approach. Both linear and nonlinear model equations are employed to build the reduced order model. The influence of different discretization methods and time steps on the ROM are evaluated. Parametric explorations are performed to investigate the capabilities of the lower-order model for predicting combustion response.

Nomenclature

PDE	=	Partial Differential Equation(s)
ODE	=	Ordinary Differential Equation(s)
ROM	=	Reduced Order Model
POD	=	Proper Orthogonal Decomposition
SVD	=	Singular Value Decomposition
FTF	=	Flame Transfer Function
FDF	=	Flame Describing Function
T	=	temperature
$\hat{a}_n(t)$	=	POD temporal coefficient
$\hat{\sigma}_n$	=	POD singular value
$a(t)$	=	POD temporal mode
$\phi(x)$	=	POD spatial mode/POD eigen-basis
N_p	=	number of POD eigen-basis included
$N_{p,\text{total}}$	=	number of POD eigen-basis in total

^{*} Graduate Research Assistant, School of Mechanical Engineering and Student Member AIAA.

[†] Professor, School of Aeronautics and Astronautics and Associate Fellow AIAA.

[‡] Professor Emeritus, AIAA Member.

[§] Senior Scientist, Rocket Propulsion Division and Senior Member AIAA.

NI = number of grid points

j = imaginary unit

Superscripts

' = perturbation variables

- = averaged/steady-state variables

Subscripts

k, n, m = POD mode #

i = # of grid point

ave = time-averaged value

I. Introduction

Combustion dynamics are a complex phenomena that results from the coupling between the modes of heat release and acoustics. In practical combustor devices the complexity is greatly amplified by turbulent, compressible flow, very high rates of heat release, and often complicated geometries and acoustic boundary conditions. Modern computational capability offers the potential for moving beyond the empirically-based design analysis of the past, but simulations of full scale dynamics for engineering analysis are still far out of reach. However, high fidelity simulations of smaller scale domains can yield reduced order models of the combustion response that can presumably provide accurate descriptions of the linear/nonlinear coupling between acoustics and combustion.

Demands for developing efficient methodologies to establish lower-order engineering models that can describe the linear/nonlinear coupling between acoustics and combustion are increasing. A hierarchy of integrated experimental and computational efforts for developing acceptable models is shown diagrammatically in Fig. 1 proposed by Portillo et al.¹ The key idea is that concurrent experiments and computations of combustion instability phenomena are used to provide high fidelity outputs from which response functions (flame models) can be derived for use in lower fidelity engineering-level testbeds.² In turn, these engineering models can be used to provide quick and reasonable predictions of the necessary physics of interest (*e.g.*, growth rate and limit cycle) in actual combustor configurations and, thereby, aid in their design evolution. Experiments provide direct/indirect measurements of physics but they are limited in the amount of information that can be output and may also have issues in the spatial and temporal resolution of the important physics. Therefore, deriving response functions from experiments can be restrictive. On the other hand, high-fidelity physics-based computations such as large eddy simulations (LES) or detached eddy simulations (DES) can provide a finely resolved description of the physics in the combustor. Therefore, they form the ideal basis for the derivation of reduced-order models (ROM), which is the subject of the present paper. We point out that that the experimental measurements are, of course, valuable as a means of validating both the high-fidelity as well as the newly developed lower-fidelity models.

The basic idea that we are exploring in this paper involves using proper orthogonal decomposition (POD) techniques to derive a reduced equation set.³ The POD is applied on the detailed simulation data to obtain a set of spatial basis vectors, which are then used within a Galerkin formulation that reduces the original partial differential equations to an ordinary differential equation. The Galerkin method has been widely used for model reduction.^{4,5} A simple example can be found in solving the classical wave equation, where Fourier series expansions are used as the eigen-bases. Instead of solving the PDE system in both time and space, after reduction, the system only needs to be solved in time. In real engineering problems, POD eigen-bases (also known as POD modes) have been widely used in computational and experimental studies of flow fields and dynamics.^{6,7} In addition, the application of POD eigen-bases for reacting flow investigations has also received attention.⁸⁻¹⁰ More importantly, POD eigen-bases have been found to be useful in model reduction of cold flow problems.¹¹⁻¹³ Moreover, reduced order models derived from incompressible flow simulations have been applied in flow control problems with classical control theories.^{3,14-16} Rowley et al.¹⁷ applied the POD-Galerkin method to compressible flow. Application of reduced order models to combustion problems has also been performed using energy and species equations.¹⁸ Munipalli et al.¹⁹ recently devised approaches for applying model reduction techniques in detailed simulations of combustion dynamics.

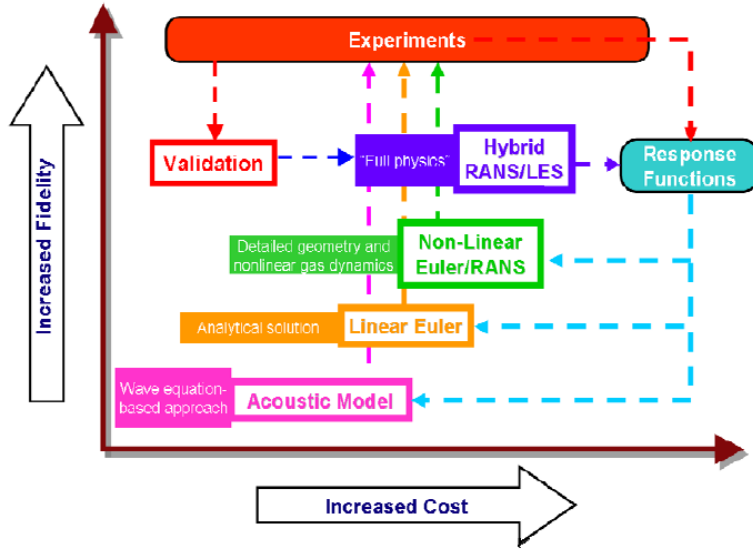


Fig. 1 Hierarchy of integrated analysis, computations and experimental work.¹

Specifically, these ideas are also related to the so-called flame transfer function (FTF) or flame describing function (FDF) described in Ref 20 and widely used in turbulent premixed flame studies in gas turbine engines.²¹⁻²³ The main difference between the FTF/FDF and the ROM approaches is that FTF/FDF characterizes the system response based on certain inputs (*e.g.*, velocity or pressure perturbations) and outputs (*e.g.*, flame perturbations) using a black-box treatment (see Ref 24). Consequently, the responses built from FTF/FDF can lose generality and are limited to certain operating conditions, combustor configurations, target frequencies, range of amplitudes, which means that, for each specific configuration or conditions, the FTF/FDF would need to be derived, tested and validated. The ROM approach provides a strong mathematical framework for such a development that has the potential to be generalized to broader conditions and configurations.

The specific objective of this paper is to demonstrate a fundamental procedure for deriving a reduced-order model formulation using a Galerkin approach based on proper orthogonal decomposition (POD) techniques for representing the spatial eigen-bases of the reduced solution. A scalar one-dimensional reaction-advection model equation is used in these studies because it captures many of the essential attributes of the combustion problem within an efficient test platform. The approach is to obtain a series of numerical solutions of the governing equation by perturbing quantities of interest such as the inlet conditions and to use the numerical solutions to build a POD eigen-basis. The POD-derived eigen-basis is, in turn, used in conjunction with a Galerkin procedure to reduce the governing partial differential equation to an ordinary differential equation which constitutes the ROM. Once the ROM is established, it can be used as a lower-order test-bed to predict detailed results within certain parametric ranges at a fraction of the cost of the full governing equations. Moreover, the ROM has the further potential to derive reduced-order response functions, which can themselves be used in the context of other reduced-physics models. The present paper is focused on the development and validation of the ROM. Application to response function derivation will be considered in future work.

The paper is organized as follows. In Section II, we present the reaction-advection equation used in the present study as well as the Galerkin formulation and POD techniques for deriving reduced order models for linear and non-linear versions of the equation. In Section III, we describe the test problem that is used in the validation studies. In Section IV, we present simulation results that demonstrate the capabilities of the reduced-order model to predict “combustion” response. Specifically, both single-frequency and broadband-forcing studies are employed in making these evaluations. In the final section, we provide some concluding remarks and future directions for continued research and development.

II. Formulation

A. Model reaction-advection equation

The heat-addition zone in combustion problems, the heat-addition zone, where the instability driving mechanisms typically originate, is characterized by a region with exponential temperature rise followed by an asymptotic relaxation to the final combustion temperature. As a representative equation for exploring the implementation of the POD-Galerkin method towards the development of a reduced order model for combustion applications, we consider the one-dimensional reaction-advection scalar equation,

$$\frac{\partial T(x,t)}{\partial t} + \frac{\partial \lambda T(x,t)}{\partial x} = k_1 \left(1 - \frac{T(x,t)}{T_f} \right) T(x,t) + k_1 \frac{T_T}{T_f} [T(x,t) - \bar{T}(x)] \quad (1)$$

In this equation, T is a temperature-like parameter (hereafter called the temperature) and λ represents the velocity with which the temperature is convected through the domain. The terms on the right hand side represent a competition between a source term that is dominant at lower temperatures and a sink that dominates at higher temperatures. The resulting solution consists of a rapid increase in temperature from an initial temperature, $T_0 = \bar{T}(0)$, followed by an asymptotic approach to a final temperature, $T_f = \bar{T}(\infty)$, a process which is characteristic of a typical combustion problem. The parameter, T_T , in the second term controls where the shift between source and sink occurs within the flame and is discussed later.

The function, $\bar{T}(x)$, in Eq. 1 is the solution to the steady version of Eq. 1 and can be obtained in analytical form as,

$$\bar{T}(x) = T_f \frac{C_1 \exp\left(\frac{k_1 x}{\lambda}\right)}{1 + C_1 \exp\left(\frac{k_1 x}{\lambda}\right)} \quad (2)$$

The constant, $C_1 = \frac{T_0}{T_f - T_0}$ is given in terms of the initial and final temperatures.

To avoid extending the computational domain over an infinite distance, we extend the domain only to a location where the temperature has very nearly reached T_f . Specifically, the length of the computational domain is chosen such that at $x = L$, the temperature at the exit of the domain is $\bar{T}(L) = (1 - \varepsilon)T_f$ where $\varepsilon \ll 1$. A typical value used for the present calculations is $\varepsilon = 1\%$. Having determined ε and L , the scaling constant, k_1 , is then given as:

$$k_1 = \frac{\lambda}{L} \ln \left(\frac{1 - \varepsilon}{\varepsilon C_1} \right) \quad (3)$$

The final parameter, T_T , in Eq. (1) is a constant to control the location of the shift between source and sink in the linearized version of the equation presented below.

Fig. 2 gives a representative family of solutions to Eq. (2) for an initial temperature of 300 and two final temperatures, 2500 and 3000 for three different values of ε , 0.5%, 1% and 2%, for each final temperature. The resulting steady state profiles have the general character of an Arrhenius term with a rapid increase followed by an asymptotic approach to the final temperature. Values of ε of 1% imply that the temperature reaches to within 1% of the final temperature in the distance $x = L$.

The following sections present solutions to the complete non-linear version as well as a linearized perturbation version of Eq. (1). The perturbed version of Eq. (1) is:

$$\frac{\partial T'(x,t)}{\partial t} + \frac{\partial \lambda T'(x,t)}{\partial x} = k_1 \left(1 + \frac{T_T}{T_f} - 2 \frac{\bar{T}(x)}{T_f} \right) T'(x,t) \quad (4)$$

where $T(x, t) = \bar{T}(x) + T'(x, t)$ and $T'/\bar{T} \ll 1$. For convenience, we represent the forcing function on the right hand side of the linearized equation as the function, G :

$$G = k_1 \left(1 + \frac{T_T}{T_f} - 2 \frac{\bar{T}(x)}{T_f} \right) \quad (5)$$

Note that G changes from a source to a sink at the particular location where $\bar{T}(x) = (T_f + T_T)/2$. When T_T is zero this transition location coincides with the inflection point in $\bar{T}(x)$. The transition location can be moved to the right by choosing positive values of T_T .

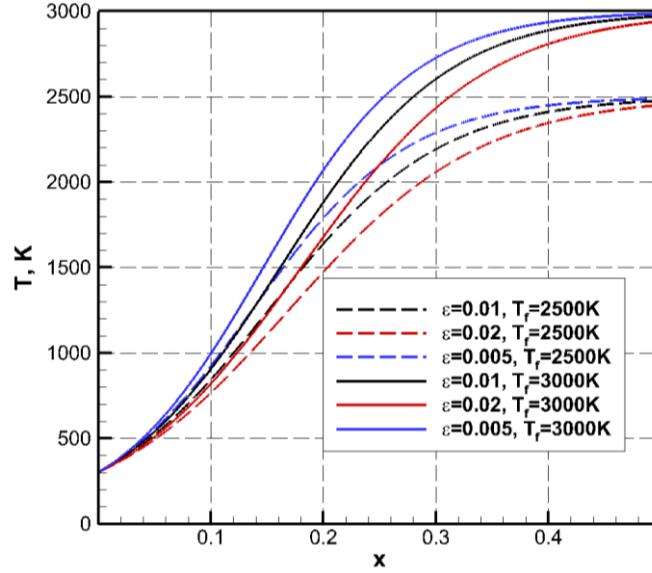


Fig. 2 Characteristics of the steady state solution, $\bar{T}(x)$ versus x , for two final temperatures and three values of ε . Solid lines, $T_f = 3000\text{K}$; dashed lines, $T_f = 2500\text{K}$ ($T_T = 0$).

B. Model Reduction using the POD-Galerkin Method

A flux-splitting, finite volume scheme with uniform cell size is used to obtain ‘high fidelity’ solutions of both the linear and nonlinear versions of the model equation. The numerical solutions are obtained by means of a second-order upwind scheme in space and a 4th-order Runge-Kutta scheme in time. For a typical computation, the numerical solution is started from the analytical steady state solution and is computed time-accurately for a sufficient number of steps with a constant flux, specified at the upstream boundary condition, until a steady numerical solution (which is near, but not exactly equal to, the analytical solution) is reached. The upstream boundary condition is then switched to a temporally varying, periodic condition, $\lambda T(0, t) = \Omega(t)$, and the time-accurate computation is continued until stationary conditions have been reached. The solution is tabulated and stored at every grid point for a large number of time steps (typically on the order of 10,000) thereby generating a rectangular matrix that can be used a data base for fitting an eigen-basis by means of the POD procedure. The POD basis vectors are then applied to the governing linear or non-linear PDE to derive the reduced-order ODE formulation. The procedure for deriving the model reductions for the linear and non-linear model equations is described in the next two sub-sections.

a. Model reduction of linearized equation

The linearized version of Eq. (1) is first used to study the implementation of the POD-Galerkin method. POD is used to represent variable $T'(x, t)$ in eigen-basis format,

$$T'(x, t) \approx \sum_{n=1}^{N_p} \hat{a}_n(t) \sigma_n \phi_n(x) = \sum_{n=1}^{N_p} a_n(t) \phi_n(x) \quad (6),$$

where σ_n is the singular value of the n^{th} POD mode, $a_n(t)$ is the n^{th} POD temporal mode and the n^{th} eigen-basis, $\phi_n(x)$, is an orthonormal function,

$$\int_X \phi_k(x) \phi_n(x) dx = \begin{cases} 1, & \text{if } k = n \\ 0, & \text{otherwise} \end{cases} \quad (7).$$

Singular value decomposition (SVD) is used to obtain the eigen-basis $\phi_n(x)$. Details of SVD applications for obtaining the POD eigen-basis can be found in Ref 25.

Upon obtaining the eigen-basis, the target governing equation is projected onto the k^{th} eigen-basis $\phi_k(x)$ throughout the whole computational domain, X ,

$$\int_X \phi_k(x) \left(\frac{\partial T'(x, t)}{\partial t} + \frac{\partial \lambda T'(x, t)}{\partial x} \right) dx = \int_X \phi_k(x) \left(k_1 \left(1 + \frac{T_T}{T_f} - 2 \frac{\bar{T}(x)}{T_f} \right) T'(x, t) \right) dx \quad (8).$$

Substituting the POD expansion, Eq. (6) into Eq. (8) gives,

$$\begin{aligned} \sum_{n=1}^{N_p} \left(\int_X \phi_k(x) \phi_n(x) dx \right) \frac{da_n(t)}{dt} + \sum_{n=1}^{N_p} \left(\int_X \phi_k(x) \frac{d\lambda \phi_n(x)}{dx} dx \right) a_n(t) \\ = \sum_{n=1}^{N_p} \left(\int_X \phi_k(x) \left(k_1 \left(1 + \frac{T_T}{T_f} - 2 \frac{\bar{T}(x)}{T_f} \right) \phi_n(x) \right) dx \right) a_n(t) \end{aligned} \quad (9).$$

Recognizing that the eigen-basis is given in tabulated form requires that these integrals be expressed as summations over the number of discrete points in the eigen-basis. For an eigen-basis tabulated at the NI cell centers of the finite volume solution, a numerical quadrature on the remaining integrals gives,

$$\begin{aligned} \sum_{n=1}^{N_p} \left(\sum_{i=1}^{\text{NI}} \phi_{k,i} \phi_{n,i} \Delta x_i \right) \frac{da_n(t)}{dt} + \sum_{n=1}^{N_p} \left(\sum_{i=1}^{\text{NI}} \phi_{k,i} \left(\frac{d\lambda \phi_n}{dx} \right)_i \Delta x_i \right) a_n(t) \\ = \sum_{n=1}^{N_p} \left(\sum_{i=1}^{\text{NI}} \phi_{k,i} \left(k_1 \left(1 + \frac{T_T}{T_f} - 2 \frac{\bar{T}_i}{T_f} \right) \phi_{n,i} \right) \Delta x_i \right) a_n(t) \end{aligned} \quad (10).$$

For notational simplicity, we have here indicated the numerical representation of the flux derivatives symbolically. Both central and upwind differences have been used in the applications. The upstream condition is obtained from the

specified boundary condition, $\lambda \sum_{n=1}^{N_p} a_n(t) \phi_{n,1/2} = \Omega(t)$, thereby providing a natural way for incorporating the boundary

condition. The flux on the downstream boundary (when needed) is obtained by extrapolation, taking into account the hyperbolic character of the equation. By separating the contributions of boundary condition explicitly as a function $F_k(\Omega(t))$, we can get,

$$\begin{aligned} \sum_{n=1}^{N_p} \left(\sum_{i=1}^{\text{NI}} \phi_{k,i} \phi_{n,i} \Delta x_i \right) \frac{da_n(t)}{dt} \\ - \sum_{n=1}^{N_p} \left(- \sum_{i=1}^{\text{NI}} \phi_{k,i} \left(\frac{\partial \lambda \phi_n}{\partial x} \right)_i \Delta x_i + \sum_{i=1}^{\text{NI}} \phi_{k,i} \left(k_1 \left(1 + \frac{T_T}{T_f} - 2 \frac{\bar{T}_i}{T_f} \right) \phi_{n,i} \right) \Delta x_i \right) a_n(t) = F_k(\Omega(t)) \end{aligned} \quad (11).$$

Here it should be noted that operator notation, $\frac{\delta(\cdot)}{\delta x}$ has been used to represent the gradient term left (uncorrelated to boundary condition) after separating the contributions of boundary term explicitly in Eq. (10) and for most of the interior cells $\frac{\delta(\cdot)}{\delta x} = \frac{d(\cdot)}{dx}$ but can be different at cells near upstream/downstream boundaries and dependent of discretization schemes used.

These steps reduce the PDE in Eqs. (1) or (4) to the system of ODE's,

$$\left\{ \begin{array}{l} M \frac{d\mathbf{a}(t)}{dt} - L\mathbf{a}(t) = \mathbf{h}(t) \\ a_k(0) = \sum_{i=1}^{NI} \phi_k(x_i) T'(x_i, t=0) \Delta x_i \quad (\text{initial conditions}) \end{array} \right. \quad (12)$$

where $\mathbf{a}(t) = [a_1(t) \ a_2(t) \ \cdots \ a_{N_p}(t)]^T$,

$\mathbf{h}(t) = [h_1(t) \ h_2(t) \ \cdots \ h_{N_p}(t)]^T$ with contributions from boundary conditions, $h_k(t) = F_k(\Omega(t))$,

M is identity matrix, ($M = I$), due to the orthogonality of POD eigen-basis.

The elements in matrix L are determined by the numerical quadrature related to $a_n(t)$ in Eq. (11),

$$l_{kn} = - \sum_{i=1}^{NI} \phi_{k,i} \left(\frac{\delta \lambda \phi_n}{\delta x} \right)_i \Delta x_i + \sum_{i=1}^{NI} \phi_{k,i} \left(k_1 \left(1 + \frac{T_T}{T_f} - 2 \frac{\bar{T}_i}{T_f} \right) \phi_{n,i} \right) \Delta x_i.$$

b. Model reduction of nonlinear equation

The application of the POD-Galerkin method to the nonlinear model equation (Eq. (1)) is very similar. The POD expansion is used to approximate the fluctuating quantity by extracting the time-averaged value from the numerical solution,

$$T(x, t) = T_{\text{ave}}(x) + T'(x, t) \approx T_{\text{ave}}(x) + \sum_{n=1}^{N_p} \hat{a}_n(t) \sigma_n \phi_n(x) = T_{\text{ave}}(x) + \sum_{n=1}^{N_p} a_n(t) \phi_n(x) \quad (13),$$

where $T_{\text{ave}}(x)$ is the time-averaged value of $T(x, t)$. Note that $T_{\text{ave}}(x)$ is the average of the non-linear solution and, in general, is not equal to the analytical function, $\bar{T}(x)$.

The same procedure can be followed from Eq. (8) to Eq. (11) to apply model reduction,

$$\begin{aligned} & \sum_{n=1}^{N_p} \left\{ \sum_{i=1}^{NI} \phi_{k,i} \phi_{n,i} \Delta x_i \right\} \frac{da_n(t)}{dt} \\ & - \sum_{n=1}^{N_p} \left\{ - \sum_{i=1}^{NI} \phi_{k,i} \left(\frac{\delta \lambda \phi_n}{\delta x} \right)_i \Delta x_i + \sum_{i=1}^{NI} \phi_{k,i} \left(k_1 \left(1 + \frac{T_T}{T_f} - 2 \frac{\bar{T}_i}{T_f} \right) \phi_{n,i} \right) \Delta x_i \right\} a_n(t) \\ & + \sum_{m=1}^{N_p} \sum_{n=1}^{N_p} \left\{ \sum_{i=1}^{NI} \phi_{k,i} \left(\frac{k_1 \phi_{n,i} \phi_{m,i}}{T_f} \right) \Delta x_i \right\} a_n(t) a_m(t) \\ & = F_k(\Omega(t)) - \left\{ \sum_{i=1}^{NI} \left(\phi_{k,i} \left(\frac{d \lambda T_{\text{ave}}}{dx} \right)_i - \phi_{k,i} \left(k_1 T_{\text{ave},i} + k_1 \frac{T_T}{T_f} (T_{\text{ave},i} - \bar{T}_i) - k_1 \frac{T_{\text{ave},i}^2}{T_f} \right) \right) \Delta x_i \right\} \end{aligned} \quad (14).$$

The reduced lower-order ODE is,

$$\begin{cases} M \frac{d\mathbf{a}(t)}{dt} - L_N \mathbf{a}(t) + \mathbf{n}(\mathbf{a}(t)) = \mathbf{h}(t) - \mathbf{b} \\ a_k(0) = \sum_{i=1}^{NI} \phi_k(x_i) T'(x_i, t=0) \Delta x_i \quad (\text{initial conditions}) \end{cases} \quad (15)$$

where $\mathbf{a}(t) = [a_1(t) \ a_2(t) \ \dots \ a_{N_p}(t)]^T$,

$\mathbf{h}(t) = [h_1(t) \ h_2(t) \ \dots \ h_{N_p}(t)]^T$ with contributions from boundary conditions, $h_k(t) = F_k(\Omega(t))$,

$\mathbf{b} = [b_1 \ b_2 \ \dots \ b_{N_p}]^T$ with contributions from time-average value $T_{\text{ave}}(x)$,

$$b_k = \sum_{i=1}^{NI} \left(\phi_{k,i} \left(\frac{d\lambda T_{\text{ave}}}{dx} \right)_i - \phi_{k,i} \left(k_1 T_{\text{ave},i} + k_1 \frac{T_T}{T_f} (T_{\text{ave},i} - \bar{T}_i) - k_1 \frac{T_{\text{ave},i}^2}{T_f} \right) \right) \Delta x_i, \quad ,$$

L_N is similar to matrix L in Eq. (12) but the time averaged value, $T_{\text{ave}}(x)$ should be used to replace $\bar{T}(x)$,

$\mathbf{n}(\mathbf{a}(t))$ is a quadratic term coming from the nonlinear term of the model equation,

$$n_k(\mathbf{a}(t)) = \sum_{m=1}^{N_p} \sum_{n=1}^{N_p} \left\{ \sum_{i=1}^{NI} \phi_{k,i} \left(\frac{k_1 \phi_{n,i} \phi_{m,i}}{T_f} \right) \Delta x_i \right\} a_n(t) a_m(t) \quad .$$

III. Overview of Test Problem

In selecting the parameters in the model equation, and the computational domain, we have chosen values that are representative of a typical combustion problem. The computational domain goes from 0 to 0.5 m $L = 0.5\text{m}$) (representative of a practical combustor length) with 1,000 uniform cells. The values of model constants (T_0 , T_f , ε and T_T) in the right-hand-sides of Eq. (1) and Eq. (4) have been selected as $T_0 = 300\text{K}$ and $T_f = 3000\text{K}$ corresponding to cold incoming reactants and a nominal flame temperature. The parameter, ε , has been set to 0.01, allowing the temperature to reach within 1% of the final temperature inside the computational domain. These three quantities yield the mean profile shown in Fig. 3. Finally, the transition temperature, T_T , has been set to 1500K, and the corresponding variation of the function, G , for the linear version (Eq. (5)) is also shown in Fig. 4. This value of T_T has been selected so that the location where G transitions from driving, $G > 0$, to damping, $G < 0$, in the linear equation occurs at $x = 0.24\text{m}$ (approximately the middle of the computational domain) as indicated by the dashed line. The same value of T_T is also used for the non-linear equation resulting in a qualitatively similar behavior. The convection velocity, λ has been set as 50 m/s, a nominal speed in a practical combustor. The time step used for numerical solution is 10^{-6} s and the solutions are output every 10 time steps (10^{-5} s).

Fluctuating conditions inside the computational domain were obtained by specifying a periodic upstream boundary condition, $\Omega(t)$, of the form,

$$\Omega(t) = \lambda T(x_{1/2}, t) = \lambda T_0 \left(1 + \varepsilon_f \frac{\sum_{k=1}^N \sin(2\pi f_k t)}{\max \left(\sum_{k=1}^N \sin(2\pi f_k t) \right)} \right) \quad (16)$$

where f_k represents the frequency of the N modes that are used in the boundary condition. The number of modes, N , used in forcing ranges from a single sinusoidal mode, $N = 1$, to a total of eight modes, $N = 8$. The peak value of the multi-frequency sinusoidal signal, $\max \left(\sum_{k=1}^N \sin(2\pi f_k t) \right)$ is used to normalize the fluctuating coefficient to make sure the total fluctuating component is ε_f of the reference value λT_0 .

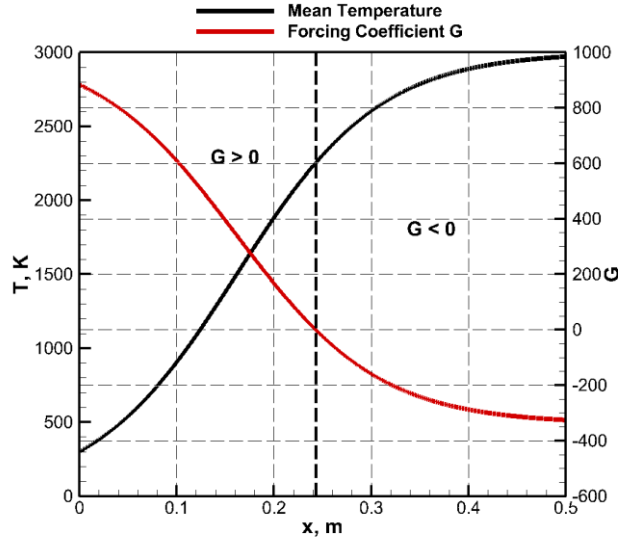


Fig. 3 Mean temperature profile and forcing coefficient G of test case ($G > 0$, driving; $G < 0$, damping).

In the results reported in the following section, we first start with solutions from the linear equation, Eq. (4) and then consider the non-linear Eq. (1). The initial examples from the linear equation provide insight without the complexities of non-linearities while the non-linear examples allow us to concentrate on any new behavior related to the non-linearity. For both linear and non-linear examples, the model reduction studies follow three distinct steps. First, we verify the POD expansion with the original CFD solution to ensure that it accurately reproduces the numerical solution. Second, we compare the ROM solution against the original CFD solution that was used to derive the POD basis vectors. This allows us to ascertain how well the ROM can reproduce the CFD solution. Third, we extend the ROM to conditions different from the original training CFD solution and then use new CFD calculations to verify the extended ROM solutions. The final test is important because this showcases how the ROM will actually be used within a design study, i.e., to investigate the effects of changes in geometric configurations and/or operating conditions.

IV. Model Reduction Studies using POD Eigen-basis

Studies of model reduction techniques are covered in this section in two parts:

1. Validation of ROM using single frequency forcing (linearized model equation)
2. Validation of ROM using broadband frequency forcing (both linearized and nonlinear model equation)

A. ROM validation using single frequency forcing

As a first step, the linear model equation (Eq. (4)) is solved by specifying a single frequency forcing at the upstream boundary. The resulting numerical solutions are then used to calculate the POD eigen-basis upon which the ROM is based. The boundary condition is perturbed at a single frequency 500Hz with $\varepsilon_f = 0.01$ (Eq.(16)) to obtain numerical solutions by solving the linearized model equation. The results at four locations are shown in Fig. 4. It is evident that the fluctuating amplitude increases as it goes downstream till the inflection point shown in Fig. 3 (i.e., the source term causes growth) and once it passes that point, the amplitude decreases (i.e., the source terms causes damping).

In the following sub-section, we first verify the solutions obtained from the POD eigen-basis. Following this, the original numerical solutions are then used to validate the reconstructed solutions from the ROM. In the next sub-section, we evaluate the robustness of the ROM procedure.

a. Verification of ROM procedure

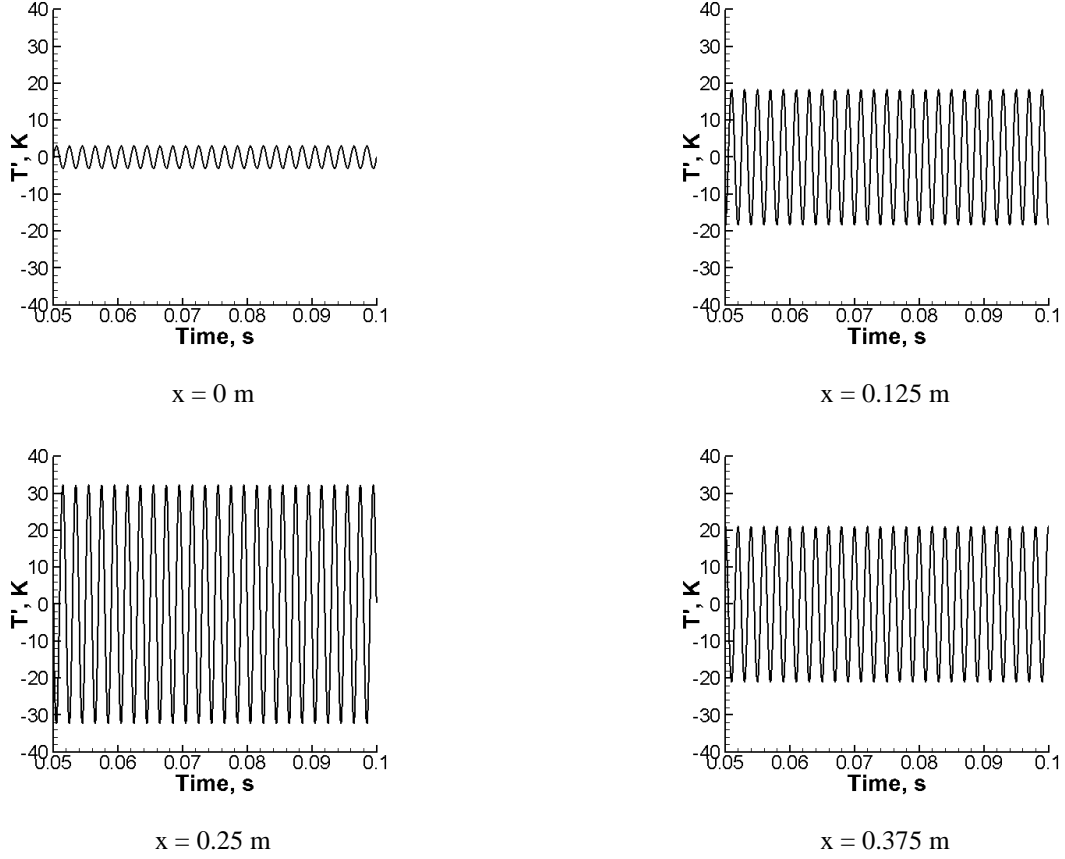


Fig. 4 CFD results from linearized model equation with 500Hz boundary perturbation at four different locations.

To investigate the quality of the POD eigen-basis, the power in any individual mode, n , (herein called the Mode Power) and the cumulative sum of the power of all modes up to N_p (the Cumulative Power) are defined based on the $\hat{\sigma}_n$ value in Eq. (6) and given as below,

$$\begin{aligned} \text{Mode Power}(n) &= \frac{\hat{\sigma}_n}{\sum_{n=1}^{N_{p,\text{total}}} \hat{\sigma}_n} \times 100\% \\ \text{Cumulative Power}(N_p) &= \frac{\sum_{n=1}^{N_p} \hat{\sigma}_n}{\sum_{n=1}^{N_{p,\text{total}}} \hat{\sigma}_n} \times 100\% \end{aligned} \quad (17).$$

where N_p is the number of POD modes used in reconstructing the solutions. These power definitions are commonly used in POD analyses. From Fig. 5(a), both the individual POD mode power and the cumulative power indicate that the first two POD modes include nearly 100% of the information in the numerical solution, while the energy content in all the higher modes is ten orders of magnitude smaller.

In addition to denoting the power in the various POD modes, we also introduce an L_2 -norm based upon the error between the eigen-basis expansion and the original CFD solution. This L_2 error provides a more sensitive assessment

of how well the reconstructed solutions represent the original CFD result. The L_2 error at any location x_i is defined as,

$$L_2\text{-norm}(N_p) = \frac{\int \left\{ T'(x_i, t) - \sum_{n=1}^{N_p} a_n(t) \phi_n(x_i) \right\}^2 dt}{\int T'^2(x_i, t) dt} \quad (18)$$

As shown in Fig. 5b, including only the first two POD modes results in an L_2 error of 10^{-8} . Interestingly, adding more modes does not decrease the L_2 error, indicating that the energy content in the higher modes for this single wave forcing problem is indeed very small. As shown later, multiple-mode forcing requires substantially more modes to reach this level of error.

It is important to note that in addition to using the L_2 -norm defined in Eq. (18) to compare the eigen-basis expansion with the original solution, it can also be used to compare the ROM solution with the CFD solution. To assess the accuracy of the ROM solution, the temporal modes, $a_n(t)$, in Eq. (18) are taken from the ROM solution (Eq. (12)), instead of from the POD expansion (Eq. (6)). In either case, the spatial modes, $\phi_n(x_i)$ are taken from the POD eigen-basis (Eq. (6)).

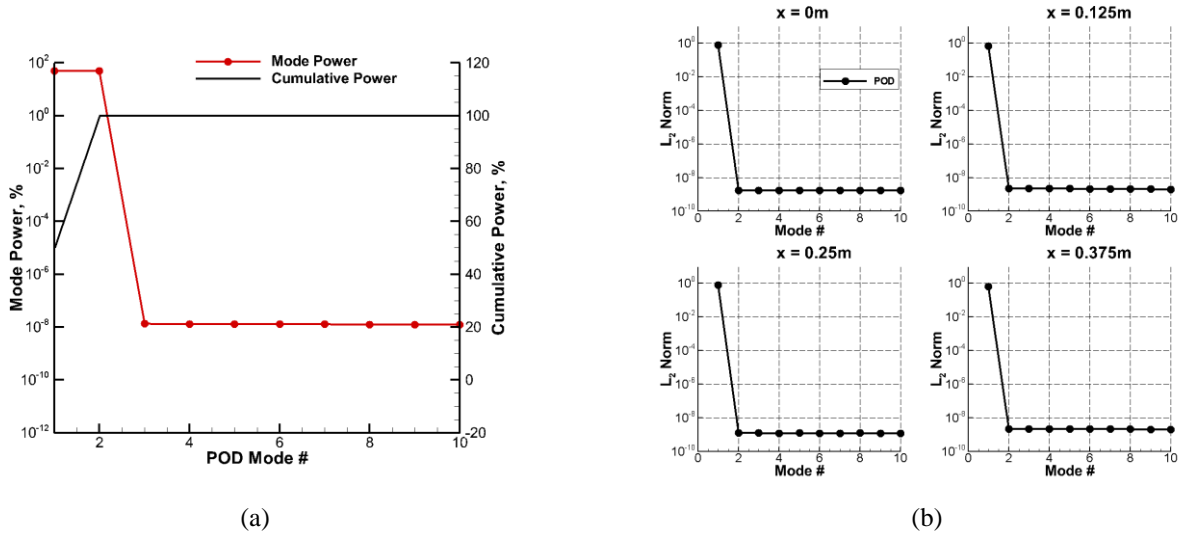


Fig. 5 Validations of POD eigen-basis from linearized model equation with 500Hz boundary perturbation (a) POD mode power & cumulative power versus mode number (b) L_2 -norm of the reconstructed solution from POD at four locations.

To characterize the reduced order model, the eigenvalues of stiffness matrix L ($\sigma + j2\pi f$ where σ is the real part indicating growth rate, j is the square root of minus one and $2\pi f$ is the imaginary part indicating the frequency, f) in Eq. (12) are calculated and shown in Fig. 6 using a 2nd-order upwind scheme to approximate eigen-basis gradient, which is consistent with the CFD solutions. With the increase of POD modes in building the ROM, the responses at the target forcing frequency (500Hz, Fig. 6(b)) are consistent ($\sigma = -1.9$) while as more POD modes are included in the ROM, responses at other frequencies show up but they are situated far from the zero-axis ($\sigma = 0$) and more importantly sit on the left half of the plane. This indicates they are all highly-damped/stable modes that have little influence on the ROM solution.

ROM calculations based upon using central differences to approximate the eigen-basis gradient in Eq. (10) are similar, but found to be inferior to upwind differencing. Similar responses at the forcing frequency are found but unlike in the case using 2nd-order upwind, as more POD modes are included, neutrally stable (near the zero axis) or even unstable modes (right half of the plane) at other frequencies show up. It is believed that this difficulty is not a characteristic of central differencing, but rather arises from using inconsistent differencing between the CFD and ROM simulations. The effect of these problematic modes on the ROM solution is covered at the end of this section.

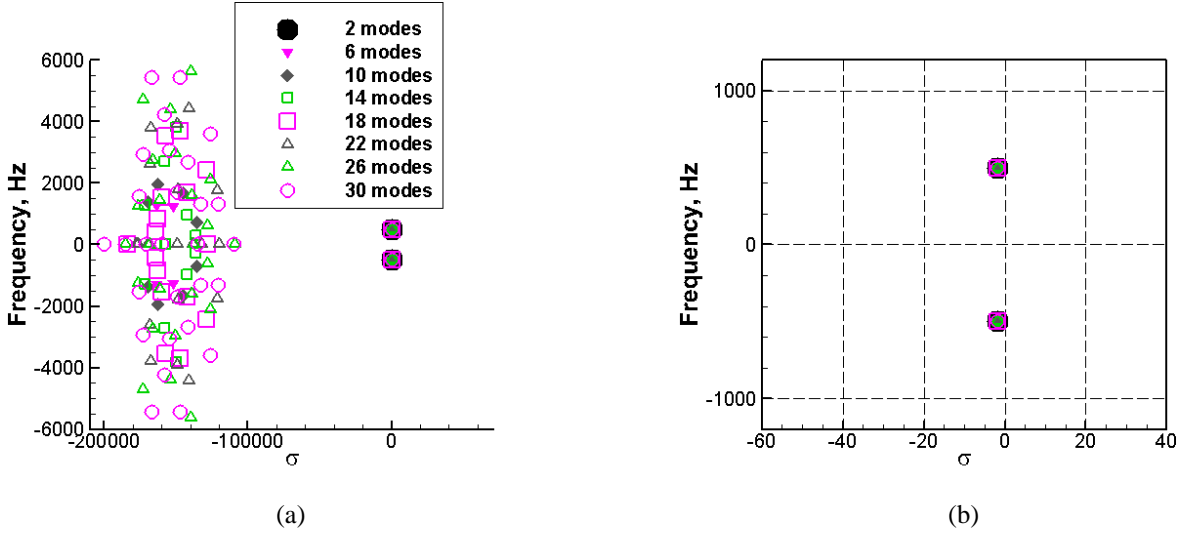


Fig. 6 Eigenvalues of the stiffness matrix L in ROM (500Hz forcing) (a) overview of all eigenvalues and (b) zoomed-in region with dominant eigenvalues ($\sigma > 0$ means unstable modes and $\sigma < 0$ means stable modes).

The reconstructed solution using ROM with one, two and five modes is compared with the CFD solution near the inflection point of the domain in Fig. 7. Here the ROM is built using 2nd-order upwind to approximate the eigen-basis gradient. The solutions are reconstructed in the same way defined in Eq. (6) but the POD temporal modes, $a_n(t)$ are calculated from the ROM (Eq. (12)) with the POD eigen-basis, $\phi_n(x)$ calculated from the CFD solutions. Consistent with the findings in the POD validation (Fig. 5), after including more than 2 POD modes, the ROM solution shows very good agreement with CFD solution.

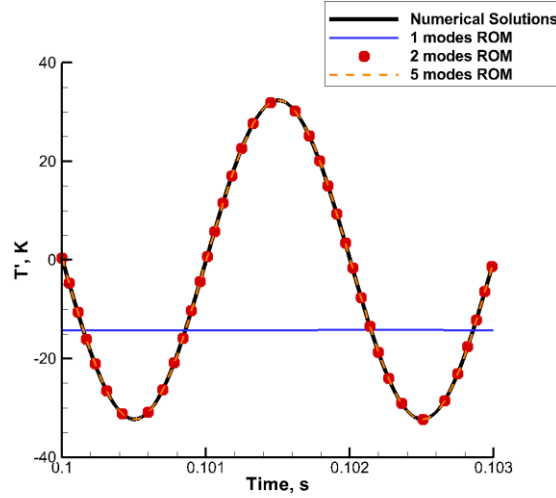


Fig. 7 Comparisons between the reconstructed ROM solutions and the CFD solutions at $x = 0.25$ m with $\Delta t = 1e-5$ s.

To provide a more quantitative assessment of how the ROM predictions compare with the CFD results we present in Fig. 8 the L_2 -norms of the ROM solution at the mid-point of the computational domain. For reference, the L_2 norm for the POD expansion, originally given in Fig. 5, is also included. Fig. 8(a) shows the L_2 norms for ROM time steps

of $\Delta t = 1e-5$ and $1e-6$ s. (Recall that the original numerical solutions were simulated with $\Delta t = 1e-6$ s while the solutions are output every 10 time steps so the POD eigen-basis are built on numerical solutions with $\Delta t = 1e-5$ s.) For both values of the ROM time step, the convergence of the ROM L_2 -norm is consistent with that from the POD norm. The error drops dramatically from the first to the second mode, but there is no further improvement when additional modes are added. There is, however, a difference in level. For a time step of $1e-5$ s, the L_2 error for two or more modes is nominally 10^{-5} while for $\Delta t = 10^{-6}$ the L_2 error is 10^{-7} . Putting this in perspective, the L_2 error for the POD expansion was 10^{-9} . These results suggest the ROM solution is second-order in time (as would be expected from the time discretization).

The L_2 norm of the error in the ROM solution also depends upon the method used for discretizing the function derivatives in Eq. (10) as can be seen by comparing Fig. 8(b) with Fig. 8(a). The results in Fig. 8(a) are based upon using a second-order accurate discretization which is consistent with that used in the CFD solution, whereas those in Fig. 8b are for central difference. The error convergence in the central difference case is qualitatively for both time-step sizes, but the levels of convergence reached are very different. The error in the central difference calculation stalls at 10^{-1} for time steps of both 10^{-5} and 10^{-6} s. The inconsistency between ROM solution using central difference and CFD solution can be attributed to the problematic neutrally stable/unstable eigen-modes mentioned above. Therefore, to build up a ROM that is able to give reasonable and comparable predictions of the physics of interest, it appears that the numerical scheme used in building the ROM should be consistent with that used in calculating the CFD solutions.

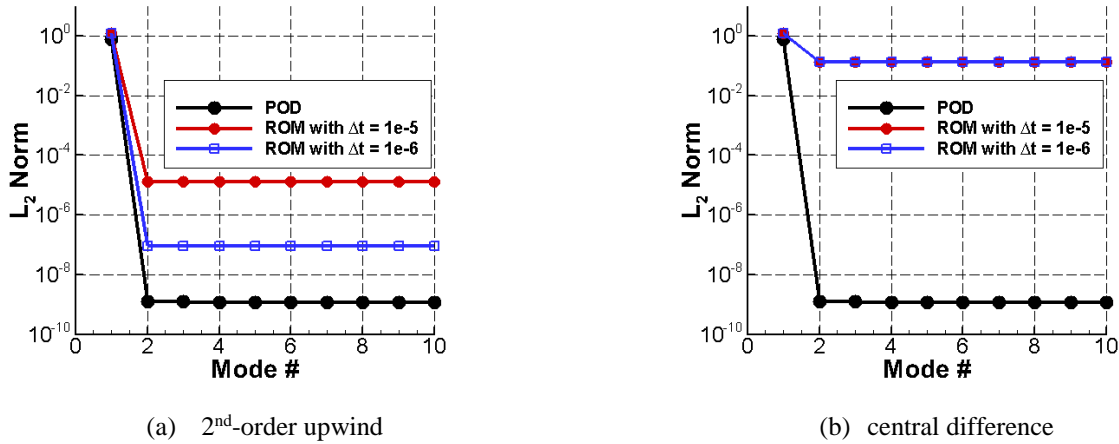


Fig. 8 L_2 -norm of the reconstructed solutions from ROM at $x = 0.25$ m using different numerical scheme in reconstructing eigen-basis at cell faces with (a) 2nd-order upwind (b) central difference.

b. Effects of time step in the ROM

To further investigate the influence of the time step size on the ROM solutions, the ROM is built from CFD solutions under a much lower frequency of excitation, i.e., 20Hz with $\varepsilon = 0.01$. The second-order upwind scheme is used in ROM to approximate the eigen-basis gradient. Different time steps are used to calculate ROM solutions. Low-frequency excitation (20Hz) is used to make sure that the time steps used can provide sufficient sample rate for the target frequency. For a 20Hz wave, a minimum sample rate of 40Hz or 0.025 s is needed to avoid aliasing. Similar POD validation procedures have been followed as in Fig. 5 and it has again been found that two POD modes are sufficient to capture the CFD solution.

In this study, two sets of POD eigen-basis have been calculated using two different sample rates (sampled every 10 time steps, $\Delta t_{pod} = 1e-5$ s and 100 time steps, $\Delta t_{pod} = 1e-4$ s) of CFD solutions respectively to build the ROM's. The eigenvalues of the ROM stiffness matrix L are shown in Fig. 9 and Fig. 10. The predictions of the responses at target frequency (20Hz) are consistent and similar to the previous case (Fig. 6). Responses at frequencies other than the driving frequency are highly damped. Though the two sets of ROM are built from different POD eigen-basis, the information delivered from the ROM's is similar.

The comparisons between the ROM solutions with different time steps and the CFD solutions are shown in Fig. 11 with $\Delta t_{pod} = 1e-5$ s. CFD solutions are compared with the ROM solution using two and four POD eigen-basis at x

= 0.25 m. In Fig. 11(a) with relatively higher temporal resolution ($\Delta t = 1e-6, 1e-5, 1e-4$ and $1e-3$ s), the predictions from the ROM by only including two POD eigen-basis follow the numerical solution well qualitatively. As the temporal resolution gets poorer, the ROM is still able to capture the same phase as the numerical solution but deviations in amplitude predictions show up ($\Delta t = 5e-3$ and $1e-3$ s). As the temporal resolution gets close to the required sample rate ($\Delta t = 2e-2$ s), the prediction from the ROM fails to follow the CFD solution. By using a ROM built from 4 POD eigen-basis (Fig. 11(b)), the ROM solutions with higher temporal resolution ($\Delta t = 1e-6$ and $1e-5$ s) reach good agreement with CFD solution while by using larger time steps, the ROM solutions fail to predict the correct behavior.

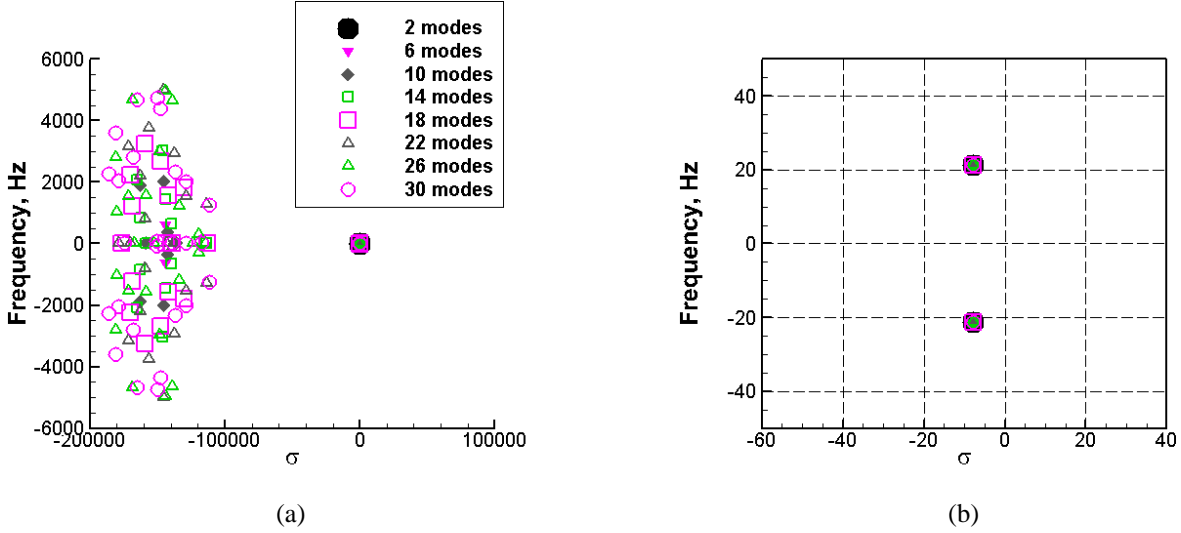


Fig. 9 Eigenvalues of the stiffness matrix L in ROM (20Hz forcing) built from POD eigen-basis calculated using CFD results sampled every 10 time steps ($\Delta t_{pod} = 1e-5$ s) (a) overview of all eigenvalues and (b) zoomed-in region with dominant eigenvalues ($\sigma > 0$ means unstable modes and $\sigma < 0$ means stable modes).

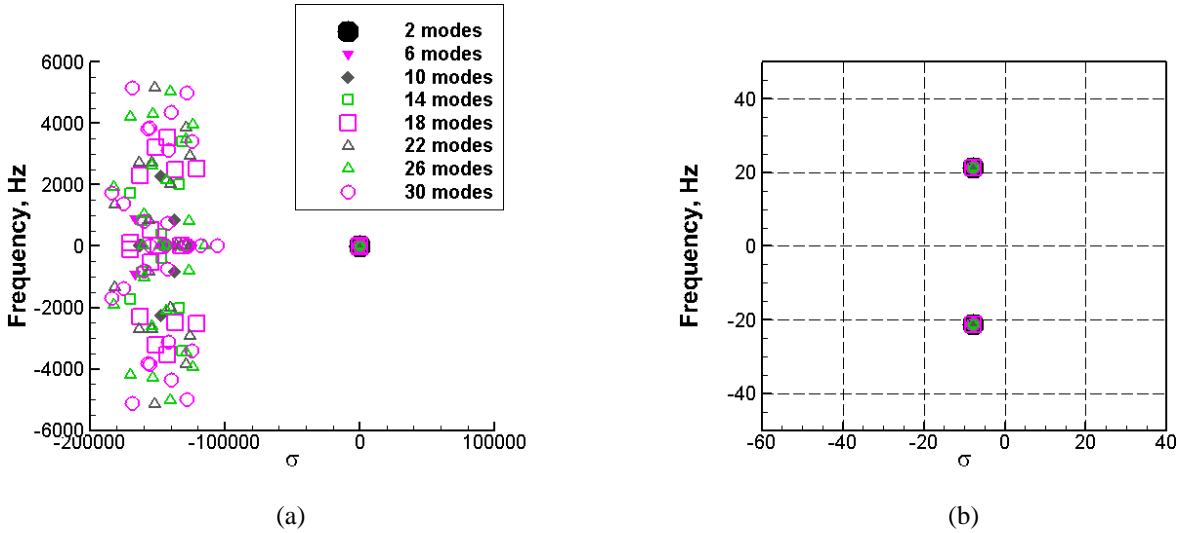
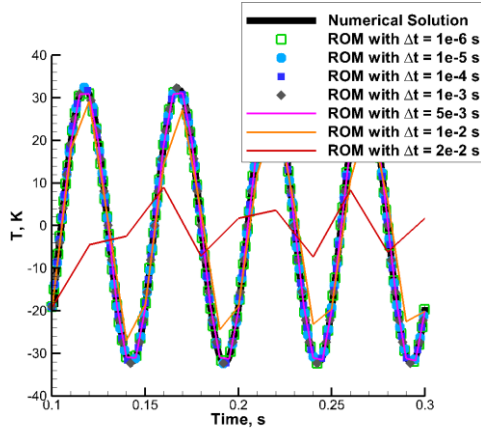
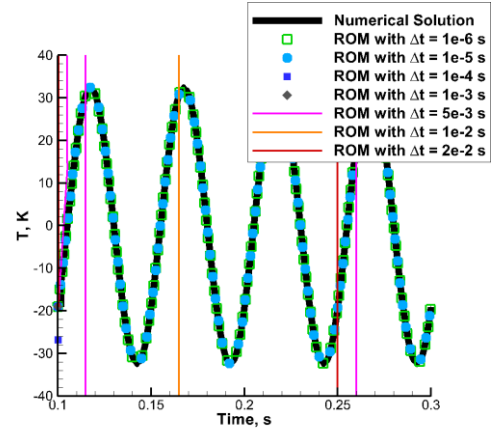


Fig. 10 Eigenvalues of the stiffness matrix L in ROM (20Hz forcing) built from POD eigen-basis calculated using CFD results sampled every 100 time steps ($\Delta t_{pod} = 1e-4$ s) (a) overview of all eigenvalues and (b) zoomed-in region with dominant eigenvalues ($\sigma > 0$ means unstable modes and $\sigma < 0$ means stable modes).



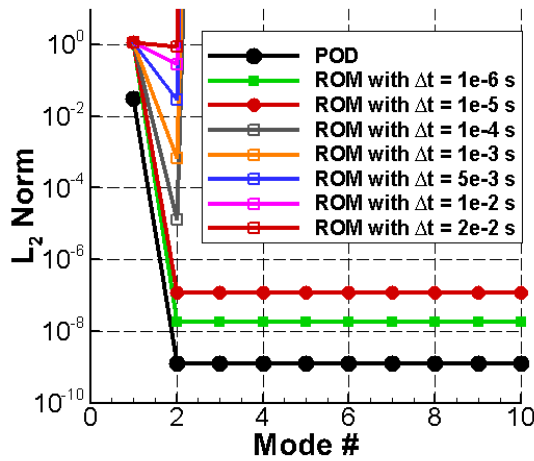
(a) Using 2 POD eigen-basis



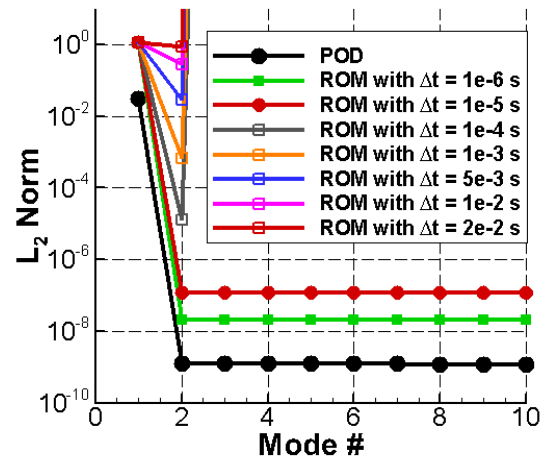
(b) Using 4 POD eigen-basis

Fig. 11 Comparisons between the ROM solutions and the CFD solution at $x = 0.25$ m with $\Delta t_{\text{pod}} = 1\text{e-}5$ s using (a) 2 POD eigen-basis (b) 4 POD eigen-basis, (c) L_2 -norm of the ROM solutions at $x = 0.25$ m with different time steps.

This can be further confirmed quantitatively by looking at the L_2 -norm of ROM solutions at $x = 0.25$ m with different time steps in Fig. 12. For time-steps larger than $1\text{e-}4$ s, the ROM's built with more than two POD eigen-bases diverge and cannot be properly used with the POD eigen-basis calculated from higher sample rate (Fig. 12(a)). Even when a lower sample rate ($\Delta t_{\text{pod}} = 1\text{e-}4$ s) is used to calculate the POD eigen-basis from the CFD solutions, the ROM solutions still diverge in the same fashion (Fig. 12(b)), which might indicate that the temporal resolution of the POD eigen-basis construction is less critical in determining the ROM predictions. However, the failure of the ROM built with more POD eigen-bases can be attributed to a lack of temporal resolution to describe those highly damped modes as shown in Fig. 9 and Fig. 10. With both sample rates, the growth rates, σ of those modes are predicted to be less than $-1,00,000$, which indicates a decay rate of $1/1,00,000 = 1\text{e-}5$ s. By including more than 2 POD eigen-bases to build the ROM, higher temporal resolution is required to capture those large decay rates.



(a) $\Delta t_{\text{pod}} = 1\text{e-}5$ s



(b) $\Delta t_{\text{pod}} = 1\text{e-}4$ s

Fig. 12 Comparisons between the ROM solutions and the CFD solution at $x = 0.25$ m with (a) $\Delta t_{\text{pod}} = 1\text{e-}5$ s (b) $\Delta t_{\text{pod}} = 1\text{e-}4$ s at $x = 0.25$ m with different time steps.

In summary of this section, reasonable predictions are obtained even when larger time steps are used for the ROM when it is built using two POD eigen-bases. However, when more than two POD eigen-bases are used then higher temporal resolution is required, ostensibly to capture the large decay rate at other frequencies.

B. ROM Implementations using broadband forcing

The studies above are all focused on the validation of the ROM. In this section, the implementation of the ROM for predicting the response at other forcing frequencies is investigated. To do that, a numerical solution is obtained with broadband forcing (200-1,000Hz with 100Hz frequency increments, Δf , and $\varepsilon_f = 0.01$) at the boundary so that the ROM built is expected to be capable of capturing the response at those frequencies. A set of separate CFD solutions has been calculated with different forcing under a range of frequencies as reference cases to test the capabilities of the derived ROM (summarized in Table 1). Both linear and non-linear cases are considered.

Case Information	Forcing frequencies, Hz
Case used to build ROM	Broadband (200-1,000Hz with $\Delta f = 100\text{Hz}$)
Test cases for ROM to predict	100
	200
	500
	1000
	200 & 500
	200, 500 & 1000
	200, 500, 800 & 1000

Table 1. Summary of cases used in studies of ROM implementations.

a. ROM trained from linear model equation

The representative CFD results for broadband forcing are shown in Fig. 13 at four locations. The multiple modes result in a periodic fluctuation that is much different from the single frequency forcing in Fig. 4, but the overall response is similar: the fluctuating amplitude grows as it goes downstream till the inflection point and decays after it passes that point.

The POD mode power and the cumulative power for this multi-frequency-forced case are shown in Fig. 14(a). It is particularly interesting to compare these results with those from the single frequency case in Fig. 5. In both the present multi-frequency case and the single mode case, there is a grouping of modes with a substantial amount of energy followed by a sudden decrease to negligible energy in the remaining higher modes. For the single frequency case, the first two modes contained nearly 100% of the energy with about 50% in each mode. For this present case, the first 18 modes contain nearly 100% of the energy, with some 10% in the first mode followed by a monotonic decay until the 18th mode contains about 1%. Modes 19 and higher all contain negligible amounts of energy. Recalling that nine modes were used to drive the present case while a single mode in the results of Fig. 5, it appears that two POD modes are required to represent each driving frequency. The cumulative power in the two cases is also consistent with this picture.

This conclusion is confirmed by the L_2 -norm of the reconstructed POD solutions in Fig. 14(b). The L_2 error remains large until a total of 18 modes have been included, at which time the L_2 error drops dramatically. Incorporating more than 18 modes provides no further decrease in the error again indicating that all the energy is represented in these first 18 modes.

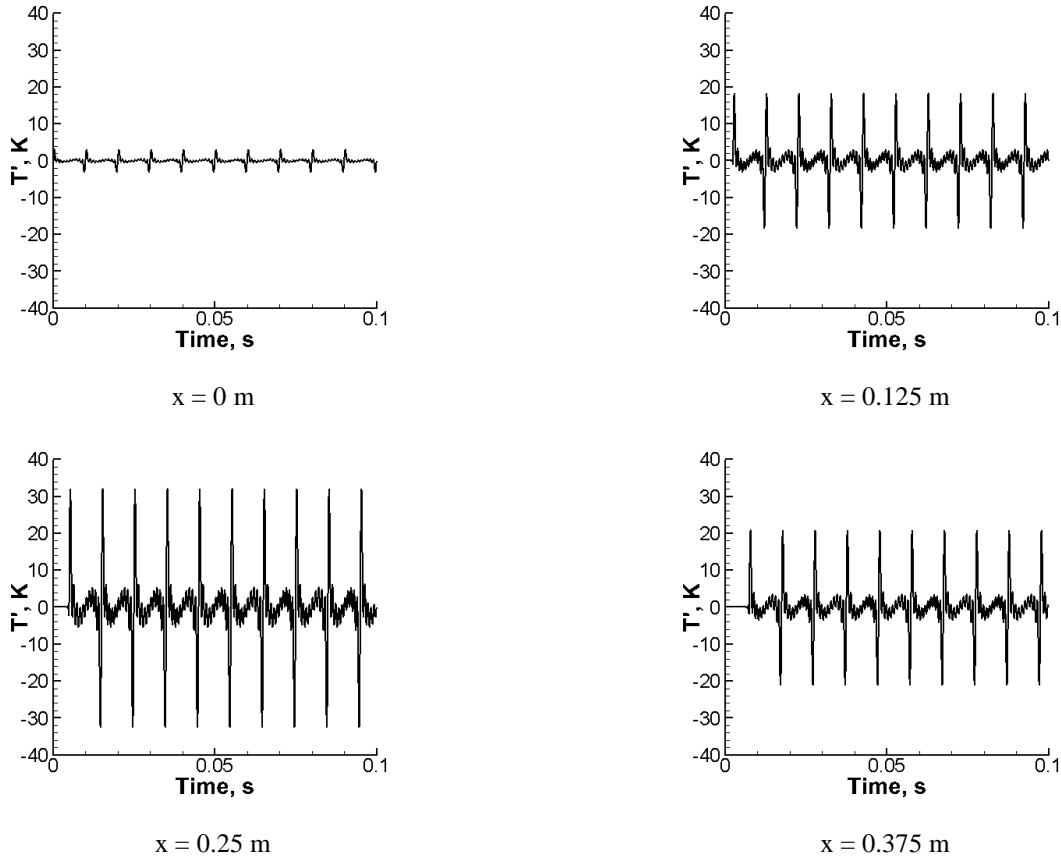


Fig. 13 CFD results from linearized model equation with broad band boundary perturbation at four different locations.

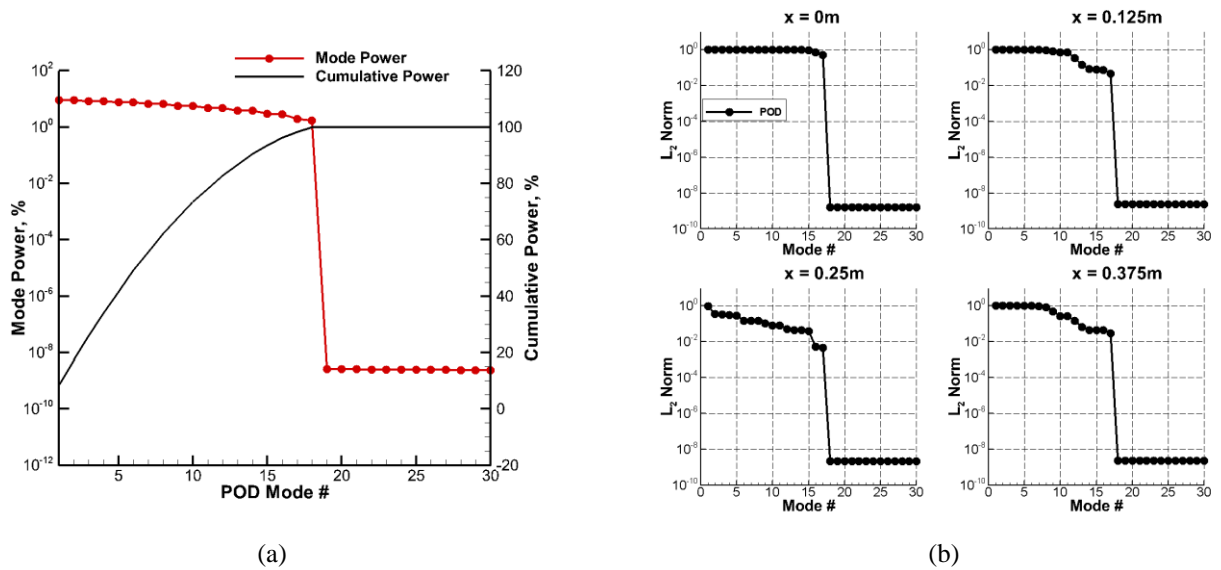


Fig. 14 (a) POD mode power & cumulative power versus mode number (b) L_2 -norm of the reconstructed solutions using POD from linearized model equation with broadband forcing.

The characteristics and validation of the ROM built from the broadband forcing are shown in Fig. 15. The eigenvalues of the stiffness matrix L (Fig. 15(a) and (b)) indicate that, by including more than 18 POD modes, the ROM predictions of responses at the target forcing frequencies become consistent. Similar to the observations made in the single-frequency cases, there are some highly-damped/stable frequencies sitting in the left plane. The L_2 -norm of the ROM solution at $x = 0.25$ m (Fig. 15(c)) also leads to similar conclusions, i.e., the inclusion of eighteen POD modes yield good convergence of the error. Again, for the smaller time step ($\Delta t = 1e-6$ s), the accuracy level of the ROM solution is improved and closer to the POD solution.

Finally, as a test to see if the ROM trained by the broadband forcing can predict the correct response for different forcing frequencies, we try the cases listed in Table 1. The different frequencies are fed to the ROM by modifying the function $\Omega(t)$ in Eq. (12) based on the definition in Eq.(16). The L_2 -norm of the ROM solutions are shown in Fig. 16 with $\Delta t = 1e-5$ s, indicating reasonable predictions for all cases except the 100 Hz forcing case. We note that the 100Hz forcing is outside the range of broadband forcing that was used to train the ROM and it is therefore expected that this case would not be represented correctly.

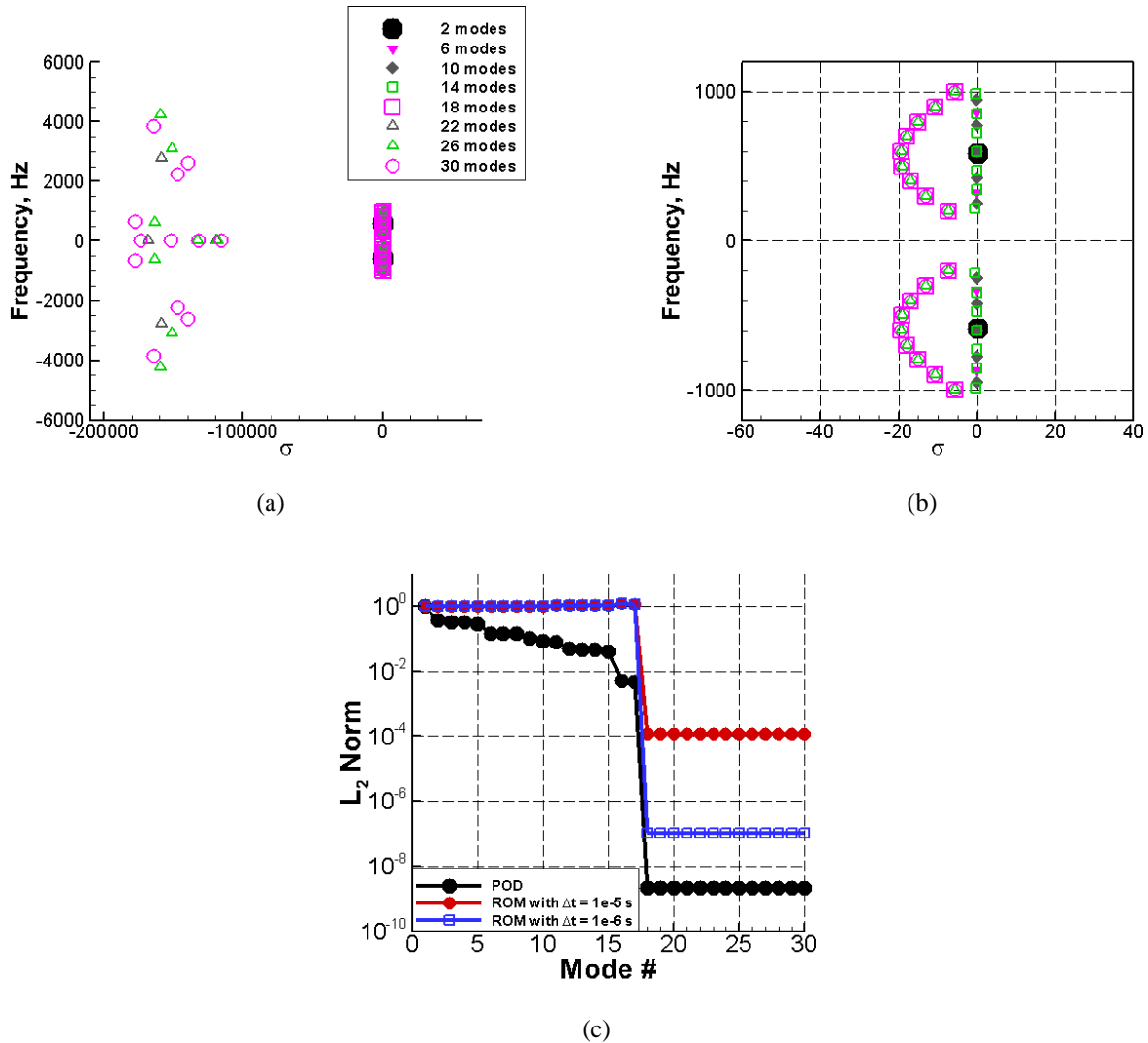


Fig. 15 Characteristics of ROM (broadband forcing) with eigenvalues of the stiffness matrix L in ROM (a) overview of all eigenvalues and (b) zoomed-in region with dominant eigenvalues ($\sigma > 0$ means unstable modes and $\sigma < 0$ means stable modes) (c) L_2 -norm of the ROM solutions at $x = 0.25$ m .

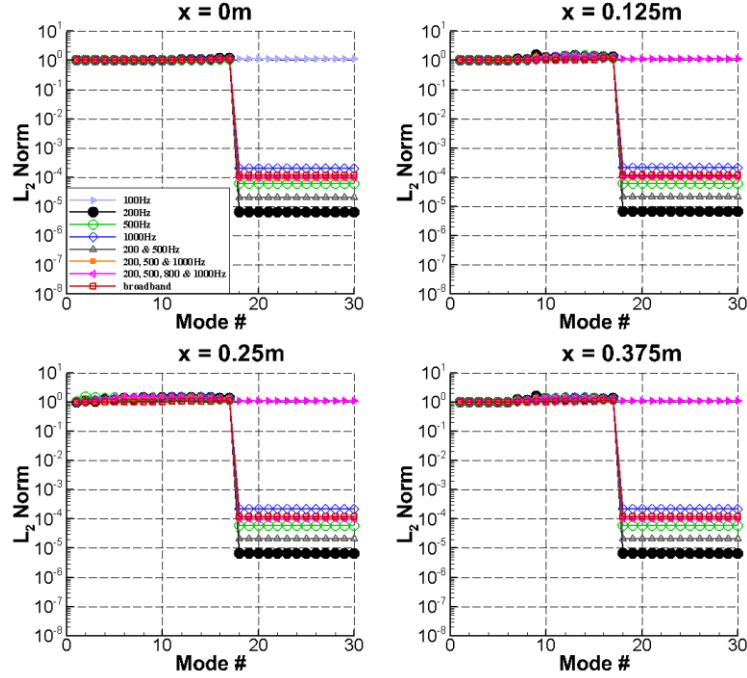


Fig. 16 L_2 -norm of the linear ROM solutions at four locations under different forcing frequencies with $\Delta t = 1e-5$ s.

b. ROM trained from nonlinear model equation

Similar to the detailed studies using the linearized governing equation, explorations of the ROM trained from nonlinear model equation are shown next. As before, broadband forcing with $\varepsilon_f = 0.01$ is used to generate numerical solutions for construction of the ROM. Representative CFD results at different locations are shown in Fig. 17. For the low amplitude forcing that is used here, the fluctuation amplitudes at each location is very close to those in the linear case (Fig. 13). Validation of the POD and the ROM are shown in Fig. 18. A big drop in mode power can be observed for POD modes higher than eighteen and the cumulative mode power reaches close to 100% (Fig. 18(a)). This can be interpreted as the inclusion of complete information to describe the linear responses, which is consistent with the finding in the linear case (Fig. 14(a)). However, unlike the linear case, the mode power is observed to keep decreasing as we go to even higher modes and saturates around 70.

The validation of the POD and ROM reconstructions shown in Fig. 18(b) can provide more quantitative understanding. The convergence of the L_2 -norms of POD and ROM is consistent with the POD mode & cumulative power. With $\Delta t = 1e-5$ s, the L_2 -norms of ROM saturate after 40 POD modes and converge by about four orders of magnitude while by using $\Delta t = 1e-6$ s, the convergence of the ROM closely follows that of the POD solution itself goes down by nearly eight orders of magnitude.

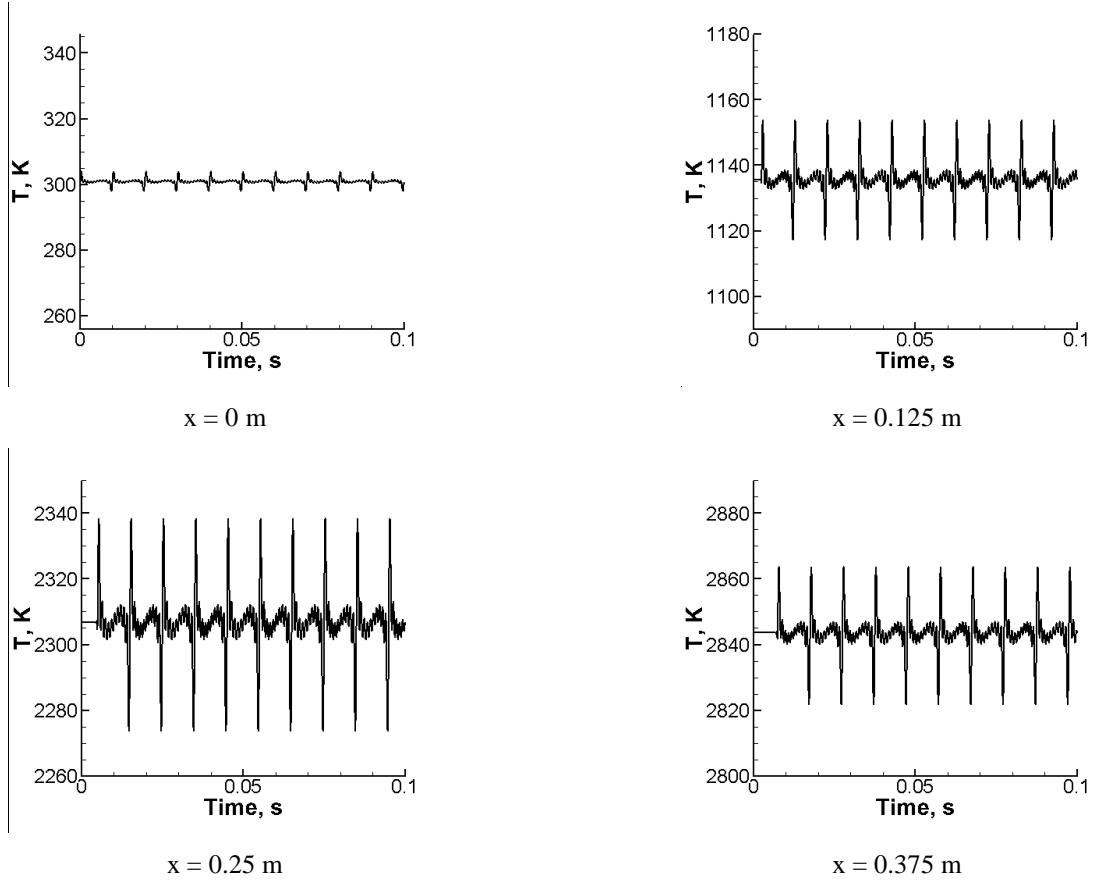


Fig. 17 CFD results from nonlinear model equation with broad band boundary perturbation at four locations.

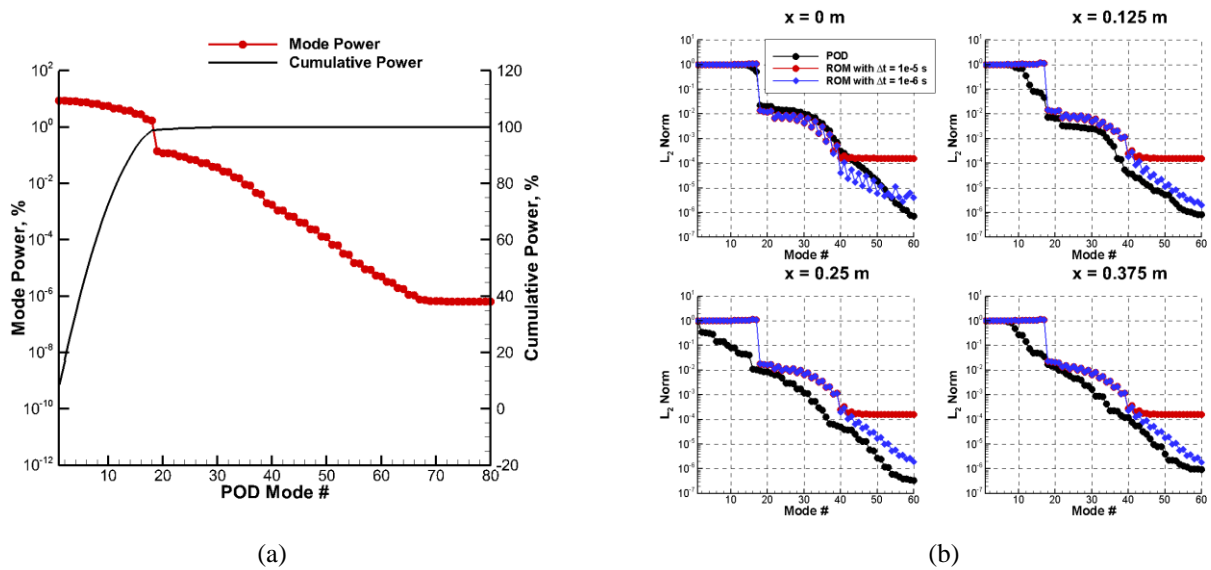


Fig. 18 (a) POD mode power & cumulative power versus mode number (b) L_2 -norm of the reconstructed solutions using POD and ROM from nonlinear model equation with broadband forcing.

As in the linear case, we next test the nonlinear ROM by forcing it with different frequencies as shown in Table 1 with the exception that we leave out the 100 Hz forcing. The L_2 -norm of nonlinear ROM solutions are shown in Fig. 19 at $x = 0.25$ m. It is noted that it takes more POD modes to reach convergence of the L_2 -norm in the nonlinear ROM than in the linear case. In Fig. 16, only 18 modes are needed to attain convergence saturation while in Fig. 19, more than 40 modes are needed to reach the saturation level. This might be attributed to the nonlinearity of the model equation. In addition, unlike the linear case (Fig. 16), where predictions of responses at other frequencies can reach better accuracy level than the reference case (broadband forcing), in the nonlinear case, the reference case achieves faster convergence and a better accuracy level. Nevertheless, we conclude that the nonlinear ROM is capable of predicting responses at different frequencies to a reasonable degree of accuracy.

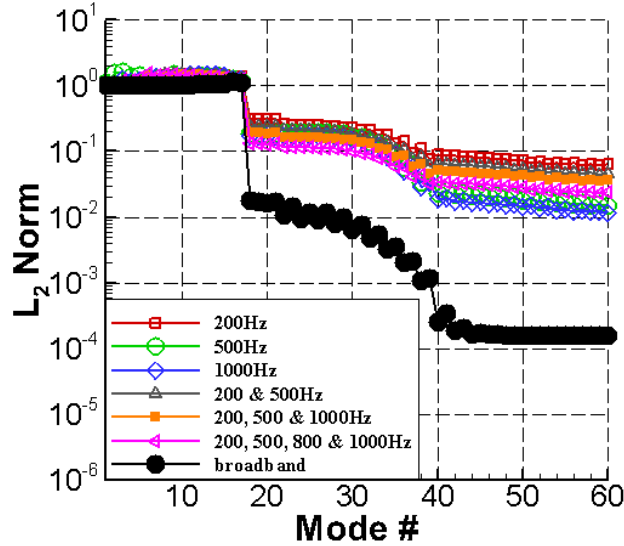


Fig. 19 L_2 -norm of the ROM solution at $x = 0.25$ m under different forcing frequencies with $\Delta t = 1e-5$ s.

For the nonlinear cases, we note that the forcing amplitude can also be a critical variable for establishing the capabilities of the ROM. To test that, the forcing amplitudes have been varied with $\varepsilon_f = 0.01, 0.02, 0.04, 0.08$ and 0.16 for the same broadband frequencies ($\varepsilon_f = 0.01$ is the reference case to build ROM).

The middle point in computation domain ($x = 0.25$ m) has been picked to compare the ROM solution and CFD solution as shown in Fig. 20. The $\varepsilon_f = 0.16$ case fails to follow the CFD solution while the other three cases ($\varepsilon_f = 0.02, 0.04$ and 0.08) capture the correct phase information with regards to the CFD solutions. $\varepsilon_f = 0.02$ and $\varepsilon_f = 0.04$ reach reasonable agreement in the fluctuating amplitudes also. But, $\varepsilon_f = 0.08$ appears to over-predict the fluctuating amplitudes. These results suggest that the ROM built using lower amplitude forcing is unable to properly resolve all of the non-linear phenomena encountered at higher amplitudes.

This information can be quantitatively represented in the L_2 -norms of the nonlinear ROM solutions for different forcing amplitudes as shown in Fig. 21. Reasonable accuracy level can be reached by including more than 40 POD modes for $\varepsilon_f = 0.02, 0.04$ and more than 50 modes for $\varepsilon_f = 0.08$ while for $\varepsilon_f = 0.16$, the nonlinear ROM predictions are observed to diverge immediately after including more than 16 POD modes. One interesting finding is that the cases with $\varepsilon_f = 0.04$ and 0.08 diverge after including more than 18 POD modes and come back to reasonable convergence when higher POD modes are included.

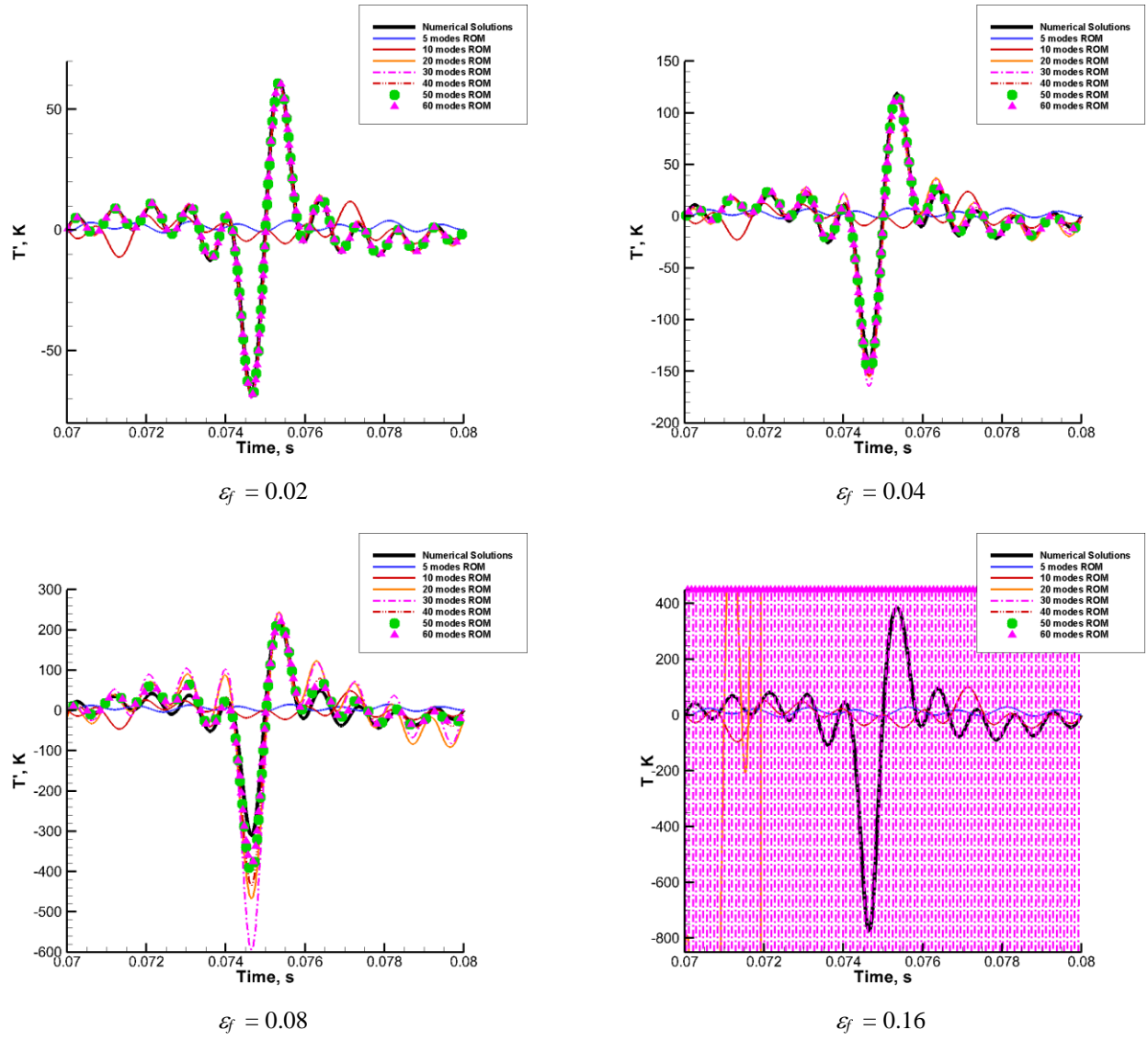


Fig. 20 Comparisons between the ROM solution and the CFD solution at $x = 0.25$ m using different forcing amplitude with $\Delta t = 1e-5$ s.

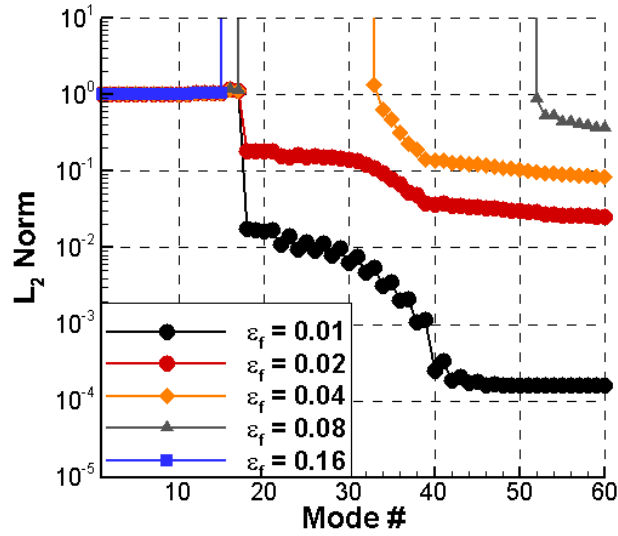


Fig. 21 L_2 -norm of the reconstructed solutions from nonlinear ROM at $x = 0.25$ m with different forcing amplitudes with $\Delta t = 1e-5$ s.

Overall, the ROMs built from the linearized and nonlinear model equation provide useful information and, more importantly, are capable of predictions of the responses for different forcing amplitude and frequencies without having to go through the solution of the full PDE model. Thus, the ROM procedure can provide substantial savings in computational time. For the calculations shown here, we estimate that the savings can be as much as 90% of the total computational time. Based on these results, we note that the ROM formulation shows significant promise for extension to more realistic systems of equations such as the Euler or Navier-Stokes equations. These extensions will be the subject of future studies.

V. Conclusions

A novel POD-Galerkin reduced-order formulation is derived and applied to a model reaction-advection equation that is representative of combustion response problems. The approach utilizes CFD solutions to obtain POD basis vectors, which are used within a Galerkin formulation to reduce the governing partial differential equations to an ordinary differential equation. The resulting ROM is verified against known solutions and its overall performance characteristics are investigated. Specifically, three steps are taken in their validation: one, the accuracy of the solution reconstructed using a certain number of POD modes is assessed; two, the accuracy of the ROM solution obtained by solving the ODE is determined by comparing with known CFD solutions for single and broadband forcing; three, the accuracy of the ROM solution to predict specific frequency response is studied using the ROM that has been trained using broadband forcing. These studies are carried out for both linear and non-linear versions of the model equation. In addition, parametric studies of the effects of time-step size, discretization method and number of POD modes on the performance of the ROM are also systematically evaluated.

The results indicate that the ROM is capable of predicting highly accurate solutions with well-converged error profiles. It is important that the discretization of the ROM follows the spatial discretization used in the original CFD solution procedure. When inconsistent discretization techniques are used, the linear matrix in the Galerkin formulation is observed to have spurious eigenvalues that prevents error convergence. For single frequency forcing, two POD modes are found to be sufficient to capture nearly 100% of the total solution, while for broadband forcing, a concomitantly larger number of POD modes are needed. Specifically, when nine discrete frequencies were used in the forcing, eighteen POD modes were required to faithfully represent the solution both with the POD and the ROM, which indicates that two POD modes are needed for each discrete frequency involved. The ROM is also found to be effective for predicting discrete frequency response when the ROM has been trained by broadband forcing. This

property is important for practical application of the ROM for design studies. It should be noted, however, that the predictions are poor when the discrete frequency is not within the range of the broadband frequencies used in the training, which is to be expected. Finally, studies are also carried out to characterize the non-linear response of the ROM solution that is trained using a low (i.e., linear) amplitude forcing. Good predictions are obtained for low forcing amplitudes, but they become poor as the forcing amplitude becomes large enough for significant non-linear effects.

Overall, the ROM demonstrates that it can be used effectively for carrying out parametric surveys of combustion response at a fraction of the cost of the full partial differential equation solution. Future studies will focus on the extension of the ROM approach to more realistic combustion physics involving the Euler and/or the Navier-Stokes equations.

Acknowledgements

The authors acknowledge the support of the NASA Marshall space flight center and technical monitor Mr. Kevin Tucker through AMA TDN/WBS Number: 10.33.1 and financial support from John Zink Company.

References

1. Portillo, J., Sisco, J., Yu, Y., Anderson, W., and Sankaran, V., "Application of a Generalized Instability Model to a Longitudinal Mode Combustion Instability" Paper 2007-5651, 43rd AIAA/ASME/SAE/ASEE Joint Propulsion Conference and Exhibit, Cincinnati, OH, July 8-11, 2007.
2. Smith, R., Xia, G., Sankaran, V., Anderson, W.E., and Merkle, C.L., "Computational Investigation of Acoustics and Instabilities in a Longitudinal-Mode Rocket Combustor", *AIAA Journal*, Vol. 46, No. 11, 2008.
3. Barbagallo, A., Dergham, G., Sipp, D., and Schmid P.J., "Closed-loop control of an open cavity flow using reduced-order models", *J. Fluid Mech.*, Vol. 641, pp. 1-50, 2009.
4. Haaskonk, B., and Ohlberger, M., "Reduced Basis Method for Finite Volume Approximations of Parametrized Linear Evolution Equations", *ESAIM: Mathematical Modeling and Numerical Analysis*, 2008.
5. Deparis, S., and Rozza, G., "Reduced basis method for multi-parameter-dependent steady Navier-Stokes equations: Applications to natural convection in a cavity", *Journal of Computational Physics*, 2009.
6. Bouhoubeiny, E., Druault, P., and Mecanique, C.R., "Note on the POD-based time interpolation from successive PIV images", *Academie des sciences*, 2009.
7. Shi, L., Liu, Y., Wan, J., "Influence of wall proximity on characteristics of wake behind a square cylinder: PIV measurements and POD analysis", *Experimental Thermal and Fluid Science*, Vol. 34, 2010, 28-36.
8. Huang, Y., Wang, S., and Yang, V., "Systematic Analysis of Lean-Premixed Swirl-Stabilized Combustion", *AIAA JOURNAL*, Vol. 44, No.4, April 2006.
9. Zong, N., and Yang, V., "Supercritical Fluid Dynamics of Pressure Swirl Injector with External Excitations", 43rd AIAA/ASME/SAE/ASEE Joint Propulsion Conference & Exhibit, 8-11 July 2007.
10. Iudiciani, P., Duwig, C., Hosseini, S.M., Szasz, R.Z., Fuchs, L., and Gumark, E.J., "Proper Orthogonal Decomposition for Experimental Investigation of Flame Instabilities", *AIAA Journal*, Vol. 50, No. 9, September 2012.
11. Lumley, J.L., and Poje, A., "Low-dimensional models for flows with density fluctuations", *Phys. Fluids*, Vol. 9, No. 7, pp. 2023-2031, 1997.
12. Sirisup, S., Karniadakis, G.E., Xiu, D., and Kevrekidis, I.G., "Equation-free/Galerkin-free POD-assisted computation of incompressible flows", *Journal of Computational Physics*, Vol. 207, pp. 568-587, 2005.
13. Wilcox, K. and Peraire, J., "Balanced Model Reduction via the Proper Orthogonal Decomposition", *AIAA Journal*, Vol. 40, No. 11, pp. 2323-2330, November 2002.
14. Barbagallo, A., Dergham, G., Sipp, D., Schmid P.J., and Robinet J., "Closed-loop control of unsteadiness over a rounded backward-facing step", *J. Fluid Mech.*, Vol. 703, pp. 326-362, 2012.
15. Herve, A., Sipp, D., Schmid P.J. and Samuelides, M., "A physics-based approach to flow control using system identification", *J. Fluid Mech.*, Vol. 702, pp. 26-58, 2012.
16. Gerhard, J., Pastoor, M., King, R., Noach, B.R., Dillmann, A., Morzynski, M., and Tadmor, G., "Model-based control of vortex shedding using low-dimensional Galerkin models", 33rd AIAA Fluid Dynamics Conference and Exhibit, June 23-26 2003, Orlando, Florida.
17. Rowley, C.W., Colonius, T. and Murray, R.M., "Model reduction for compressible flows using POD and Galerkin projection", *Physica D*, Vol. 189, pp. 115-129, 2004.
18. Huang, W.T., and Baumann, X., "Reduced-order modeling of dynamic heat release for thermoacoustic instability prediction", *Combustion Science and Technology*, Vol. 179, No. 3, pp. 617-636, 2007.

19. Munipalli, R., Liu, Z., Zhu, X., Menon, S., Hesthaven, J.S., “Model Reduction Opportunities in Detailed Simulations of Combustion Dynamics”, *52nd Aerospace Sciences Meeting, 13-17 January 2014, National Harbor, Maryland*.
20. Noiray, N., Durox, D., Schuller, T., and Candel, S., “A unified framework for nonlinear combustion instability analysis based on the flame describing function”, *J. Fluid Mech.*, 625: 139-167, 2008.
21. Bellows, B.D., Forte, A., Bobba, M.K., Seitzman, J.M., and Lieuwen, T., “Flame transfer function saturation mechanisms in a swirl-stabilized combustor”, *Proceedings of the Combustion Institute*, 31:3181-3188, 2007.
22. Bellows, B.D., Bobba, M.K., Forte, A., Seitzman, J.M., and Lieuwen, T., “Nonlinear flame transfer function characteristics in a swirl-stabilized combustor”, *Journal of Engineering for Gas Turbines and Power*, 129:954-961, October 2007.
23. Palies, P., Durox, D., Schuller, T., and Candel, S., “*The combined dynamics of swirler and turbulent premixed swirling flames*”, *Combustion and Flame*, 157:1698-1717, 2010.
24. Urbano, A., Schulze, M., Zahn, M., Schmid, M., Sattelmayer, T., and Oschwald, M., “Investigations on Thermoacoustic Feedback on a Representative Test Chamber Configuration”, *Sonderforschungsbereich/Transregio 40 – Summer Program Report* 2013.
25. Chatterjee, A., “An introduction to the proper orthogonal decomposition”, *Current Science*, Vol. 78, No. 7, 10 April 2000.